Relationship Between Microstructure, Strength, and Fracture in an Al-Zn-Mg Electron Beam Weld: Part II: Mechanical Characterization and Modeling

Quentin Puydt, Sylvain Flouriot, Sylvain Ringeval, Frédéric de Geuser, Rafael Estevez, Guillaume Parry, Alexis Deschamps

Relationship Between Microstructure, Strength, and Fracture in an Al-Zn-Mg Electron Beam Weld: Part II: Mechanical Characterization and Modeling

QUENTIN PUYDT, SYLVAIN FLOURIOT, SYLVAIN RINGEVAL, FREDERIC DEGEUSER, RAFAEL ESTEVEZ, GUILLAUME PARRY, and ALEXIS DESCHAMPS

This paper presents an experimental and modeling study of the mechanical behavior of an electron beam welded EN-AW 7020 aluminum alloy. The heterogeneous distribution of mechanical properties is characterized by micro-tensile tests and by strain field measurements using digital image correlation technic. These results are related to the microstructural obser-vation presented in the companion paper. The mechanical behavior of the weld is simulated by a finite element model including a Gurson-type damage evolution model for void evolution. The model is shown to be capable of describing accurately experimental situations where the sample geometry is varied, resulting in stress triaxiality ratios ranging from 0.45 to 1.3.

I. INTRODUCTION

PRECIPITATION hardening aluminum alloys are commonly used for structural applications requiring high specific strength, particularly in all transportation sectors (such as automotive and aerospace). Many techniques exist for assembling such alloys. Although solid-state techniques such as friction stir welding appear very attractive to retain the potential for precipitation hardening in all the weld regions, in many cases it remains desirable or necessary to use fusion techniques, such as gas metal arc welding (GMAW), metal inert gas welding (MIG), laser beam welding (LBW), or electron beam welding (EBW). An extensive review of these different techniques, applied on different alloys, can be found in Reference 1. Among precipitation hardening aluminum alloys, the EN-AW 7020 is a medium strength Al-Zn-Mg alloy particularly suited to welding,[2–4] due to the absence of Cu addition and to the low quench sensitivity related to the relatively low solute content.

QUENTIN PUYDT, formerly Ph.D. Student with the SIMAP Laboratory, Université Grenoble Alpes, 38000 Grenoble, France, also with the CNRS, SIMAP, 38000 Grenoble, France, and also with the CEA Valduc, 21120 Is-Sur-Tille, France, is now Research Scientist with the IRT M2P, Metz, France. SYLVAIN FLOURIOT and SYLVAIN RINGEVAL, Research Scientists, are with the CEA Valduc. FRÉDÉRIC DE GEUSER, Research Scientist, is with the SIMAP Laboratory, Université Grenoble Alpes, and also with the CNRS, SIMAP. RAFAEL ESTEVEZ, Professor, is with the SIMAP Laboratory, Université Grenoble Alpes, also with the CNRS, SIMAP, and also with the Université Joseph Fourier, Saint-Martin-d'Héres, France. GUILLAUME PARRY, Associate Professor, and ALEXIS DESCHAMPS, Professor, are with the SIMAP Laboratory, Université Grenoble Alpes, also with the CNRS, SIMAP, and also with the Grenoble Institute of Technology, Grenoble, France. Contact e-mail: alexis.deschamps@grenoble-inp.fr

Irrespective of the welding technique, the assembly of precipitation hardening aluminum alloys always results in a heterogeneous spatial distribution of mechanical properties. Depending on the welding technique (whether it implies fusion and subsequent solidification), on the presence of filler material, on the initial temper and possibility of post-welding heat treatment, the softest zones can be found in the weld nugget or in the heat-affected zone.

Accounting properly for the presence of the weld in mechanical design is a complex problem. The elasto-plastic mechanical behavior of the weld assembly is the result of the spatial distribution of the constitutive laws of the different zones affected by the welding operation. In addition, describing the behavior until fracture requires the knowledge of the fracture mechanisms in the zone where damage will develop first (usually the softest zone of the assembly), which is coupled to the elasto-plastic behavior of the assembly, in particular through the value of the hydrostatic stress which depends strongly on the spatial distribution of strength and sample geometry.

Therefore, developing a model for describing the mechanical properties until fracture of a weld assembly brings several requirements:

- A spatially resolved description of the microstructure within the different zones of the weld, both at the scale controlling the elasto-plastic behavior (nanometer scale of precipitation) and at the scale controlling the fracture behavior (micrometer scale of damage initiation).
- A spatially resolved description of the constitutive laws resulting from these microstructures.
- A finite element model including these constitutive laws as well as a model describing the damage evolution and fracture.

In order to assess the robustness of such a model, it needs to be applied to cases where the material is subjected to a variety of stress states.

Such approaches have already been proposed for welding of aluminum alloys, with various levels of integration from the microstructure till the fracture. A large number of papers can be found that relate the local distribution of mechanical properties to the elasto-plastic behavior of the weld assembly using finite element modeling without accounting for fracture.[5–10] Local approaches to fracture based on the Gurson–Tvergaard–Needlemann model for ductile failure and its extensions,[11–17] have long been implemented in Aluminum alloys and their welds, essentially but not exclusively in the context of friction stir welding.[18–26] For friction stir welded Aluminum alloys, a fully integrated modeling approach has been developed and applied to 6000 series alloys.[27]

Electron beam welded assemblies of aluminum alloys have been the subject of a significant number of studies[3,28–49] on all aspects of processing, resulting microstructures, and distribution of properties. This welding technique is characterized by a high penetration depth and low heat input, which results in a narrow welded nugget and limited extension of the heat-affected zone.[40] The small grain size, fast solidification rate, and clean welding environment result in very good mechanical properties including toughness,[36,41] although some solute loss due to fusion under vacuum is generally observed.[35,39] Electron beam welds are characterized by strong spatial gradients of microstructure and mechanical properties as compared to other welding techniques. In addition, the weld nugget shows a solidification microstructure, resulting in a specific distribution of solute at the microscopic level and in the presence of intermetallic phases that may control the fracture behavior. To our knowledge, there is so far no modeling study of the mechanical behavior of such welds including the effect of microstructure on the distribution of mechanical properties and ductile fracture.

In a companion paper,[50] the microstructure of electron beam welds of EN-AW 7020 alloy has been described in detail using a spatially resolved, multi-scale approach. In this paper, the microstructure after EBW was investigated both in the naturally aged state (welding followed by aging at room temperature) and after a post-welding heat treatment (PWHT). The latter will be now investigated for its mechanical behavior. After PWHT, the microstructure state of the heat-affected zone (HAZ) and associated hardness distribution is relatively homogeneous, similar to that of the base material. In the region of the HAZ closest to the fusion zone, a new precipitate size distribution has formed, similar to that present in the base material. Further from the fusion zone, a slightly coarser precipitate microstructure has been identified, relating to a coarsening mechanism that occurs during welding. However, the extent of the observed coarsening was very limited owing to the fast heating and cooling rate of the EBW process, and did not result in a significant hardness dip. In contrast, the microstructure of the fusion zone is very different from the rest of the assembly. It is affected by solute evaporation (mostly Zn but also Mg), and this smaller amount of solute is heterogeneously distributed at the scale of the solidification microstructure. In the inter-dendritic regions, the precipitate distribution after PWHT is similar to that of the base material, however at the core of the dendrites the microstructure is completely free of precipitates. This heterogeneous distribution of solute is shown to result in very low hardness, actually lower than what would be expected from the same amount of precipitates if they were homogeneously distributed. In addition, the fusion zone contains a distribution of constituent phases (Fe-containing intermetallics) that is very different from the base material. These take the form of equiaxed aggregates of loosely packed nano-crystals, present in the inter-dendritic regions.

The aim of the present paper is to propose a characterization and modeling approach, based on this microstructural study, to describe the mechanical behavior of these electron beam welds. Special attention will be paid to assess the robustness of the model by studying sample geometries that span a large range of conditions of stress states. The elasto-plastic behavior will be modeled based on the local constitutive laws characterized by micro-tensile samples at different locations throughout the weld. The fracture behavior will be described using a Gurson-type model that will be included in the finite element model.

II. MATERIALS AND METHODS

The chemical composition of the EN-AW 7020 Aluminum alloy used in this study is (in weight percent): 4.65 pct Zn, 1.25 pct Mg, 0.02 pct Cu, 0.11 pct Mn, 0.28 pct Cr, 0.09 pct Fe, 0.04 pct Si, 0.13 pct Zr, and 0.04 pct Ti. The alloy was received as a forged bar in a peak aged T652 temper.

Plates of 7 mm in thickness and 10×5 cm^2 in size were machined from the base metal, so that the forging direction was the short transverse direction of the plate. These plates were butt welded in Alcatel® high vacuum equipment, with energy per unit of length equal to 150 kJ m^{-1}. Once assembled, the welded plates formed a unique plate of 10×10 cm^2. The penetration depth of the weld was comprised between 5 and 5.5 mm. After welding, the weld was kept 15 days at room temperature for natural aging followed by 48 hours at 423 K (150 °C) (ramp heating 80 K h^{-1}).

Transverse tensile tests were carried out normal to the weld direction on samples with a 60 mm gauge length, 3 mm thickness, and variable width of 3, 7, or 30 mm. The tests were carried out with displacement control at a rate of 0.025 mm s^{-1}. The distribution of strain was measured using digital image correlation with the Aramis software.

The local stress–strain curves of the different zones of the weld were obtained by micro-tensile samples prepared by electro-discharge machining and subsequent polishing. Their gauge dimension was 15 mm length, 3 mm wide, and 0.8 mm thick.

Kahn tear tests were carried out according to ASTM B781-01 (2007). The sample thickness was 3 mm and the

ligament was 25 mm long. The test was carried out under displacement control at 0.025 mm s^{-1}. The load and opening displacement are recorded during the test.

Fractography analysis was carried out using a standard scanning electron microscope LEO Stereoscan 440 at 20 kV. High resolution images were obtained on a Zeiss Ultra-55 FEG-SEM at 4 kV with in-lens secondary and back-scattered detectors. Finite element modeling was carried out using the ABAQUS software in the explicit mode for the damage calculations and failure.

III. MECHANICAL BEHAVIOR OF THE WELD ASSEMBLY

We first consider the case of a transverse tensile test performed on the weld, with a sample of cross-section 7 × 3 mm. The distribution of plastic deformation across the weld zones during the tensile test is followed by digital image correlation in the plane normal to the welding direction (3 mm width). Figure 1 presents the nominal stress–strain curves of the base material as a reference, and that of the weld with a reference length of 20 mm (comprising both the weld nugget and the heat-affected zones) and of 3 mm (comprising only the weld nugget). As expected from the distribution of hardness in the weld, which presents a pronounced dip in the nugget (see companion paper[50]), the yield strength of the assembly is much lower than that of the base material, and then plasticity localizes quickly in the nugget region. The apparent strain hardening rate of the weld assembly is extremely high, reflecting the elasto-plastic transition and the effect of constrained plasticity. The weld nugget presents a large ductility before failure, actually quite larger than that of the base material.

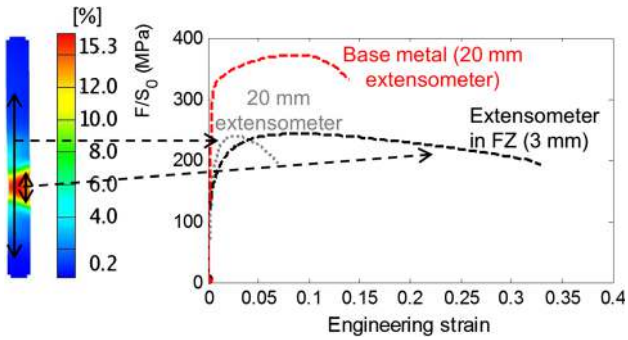

Fig. 1—Nominal stress–strain curves of the base material and of the transverse weld assembly. The map of plastic deformation as measured for the weld assembly by digital image correlation is shown. The two nominal stress–strain curves for the weld are obtained using respectively a gauge length of 3 mm within the fusion zone and of 20 mm across the different weld zones.

Figure 2 shows the distribution of strain as measured by digital image correlation across the weld at three points of the load-displacement curve: (1) close to the onset of plasticity, (2) at maximum load of the weld assembly, and (3) close to failure. In the three cases, the plastic deformation is fully localized in the weld nugget, and the remaining material remains elastic.

Figure 3(a) shows the fracture surface of the transverse welded sample. The fracture is uniformly ductile with relatively monodisperse and homogeneously distributed dimples whose sizes are in the micrometer range. At higher magnification, small equiaxed intermetallic particles can be observed at the core of these dimples (Figure 3(b)). These correspond well to the phases resulting from the end of solidification (see Figure 3(c)), which are present in the inter-dendritic regions. In the companion paper it was shown that these regions were made of a collection of loosely packed nanocrystals, which is consistent with them serving as nuclei for ductile damage initiation.

We have now identified that the main damage mechanism during the transverse weld testing is the nucleation and growth of voids. One critical parameter that influences this mechanism is the stress triaxiality ratio, and therefore it is critical to be able to vary this parameter to assess the robustness of the mechanical model that will be presented further in the paper. For this purpose, transverse welded samples of different

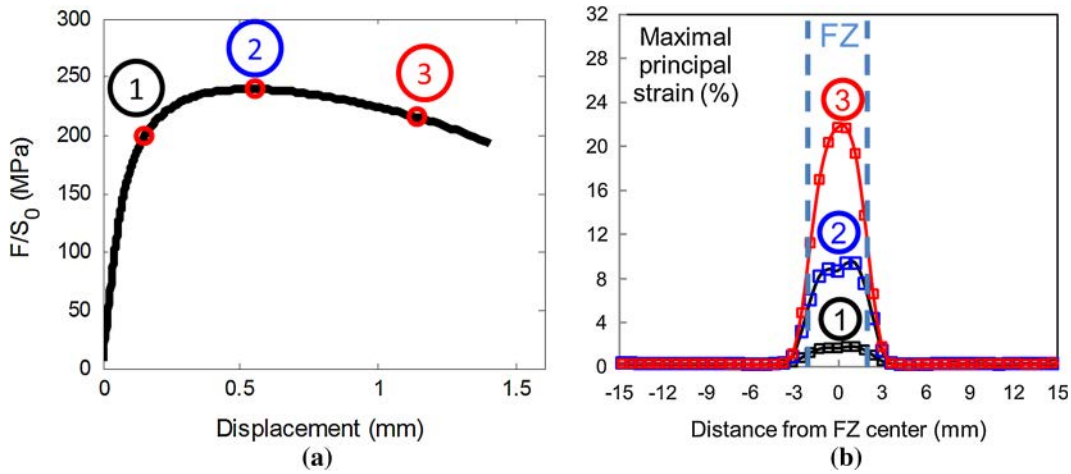

Fig. 2—(*a*) Nominal stress–displacement curve for the weld assembly; (*b*) strain distribution measured by digital image correlation at three stages of the test as defined in (a).

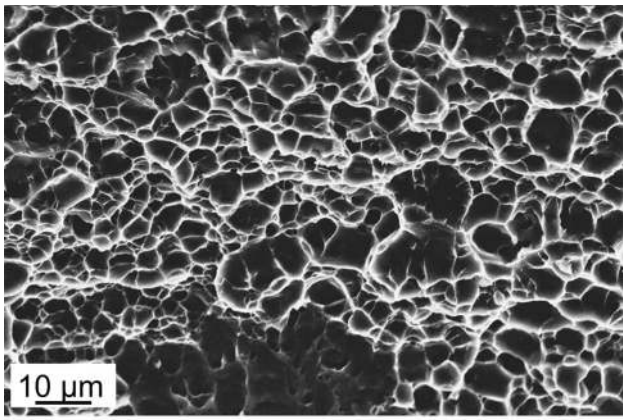

(a)

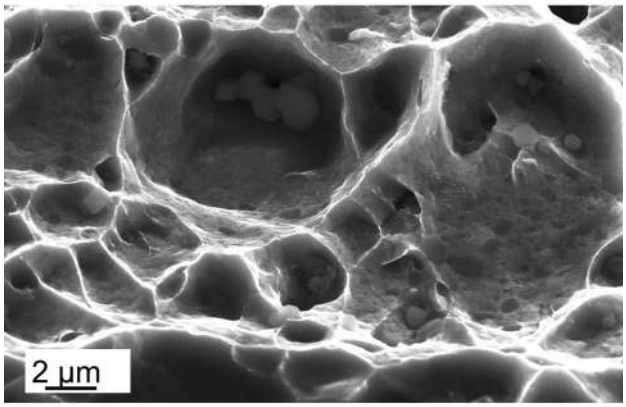

(b)

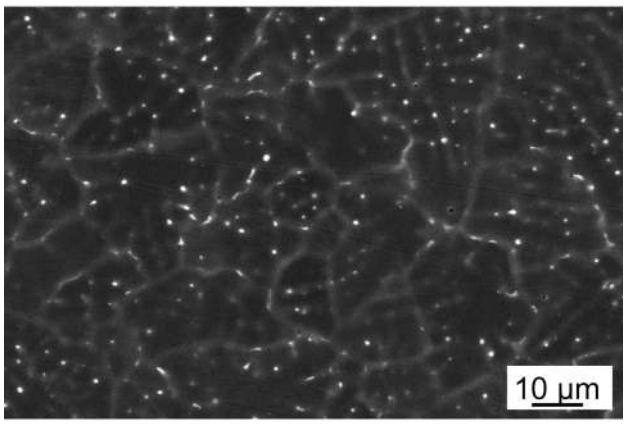

(c)

Fig. 3—(*a*) Fracture surface of the transverse tensile test showing the ductile nature of the fracture surface in the weld nugget; (*b*) detail of the dimples showing the presence of a distribution of very fine intermetallic particles; (*c*) back-scattered image of a polished section of the weld nugget showing the distribution of intermetallic particles resulting from the solidification process.

geometry have been tested. The thickness of the samples being kept constant at 3 mm, the width was varied from 3 to 30 mm, resulting in a varying constraint on the soft nugget zone from the harder base material.[6] The evaluation of stress triaxiality ratio as a function of sample geometry requires the finite element model of the weld assembly and will therefore be shown later in the paper. However, it can be qualitatively expected to increase together with the sample width. Figure 4(a) shows the load-displacement curves for the three samples of different geometry. As expected, the higher triaxiality ratio resulting from a larger sample width results in a higher strength and lower ductility, due to accelerated damage growth. Figures 4(b), (c), and (d) compare the fracture surfaces for the three samples. In all three cases the fracture mechanism is the same, namely fully ductile. Moreover, the size of the dimples is not appreciably different between the different samples. This suggests that the damage initiation sites are the same regardless of the applied stress state, consistently with the distribution of intermetallic particles in the material.

IV. ELASTO-PLASTIC MODELING

A. *Micro-tensile Tests*

In order to obtain the local constitutive laws, specimens of small sizes (0.8×3 mm^2 rectangular section and 15 mm in effective length) were extracted from different zones of the weld, parallel to the weld direction. The specimens in the heat-affected zone (HAZ) were machined with an angle of 20 deg to correspond to the shape of the fusion zone (FZ). Samples were cut in the FZ as well as from 6 to 8 mm from the fusion zone center and the nominal stress/strain curves are plotted in Figure 5.

The stress–strain curves in the different parts of the HAZ are observed to be very similar, consistently with the hardness distribution shown in the companion paper.[50] As expected, the sample at 6 mm shows a slightly lower strength, which corresponds to the region of partial dissolution and coarsening during welding. The stress–strain curve of the fusion zone shows a much softer behavior. The analysis of the microstructure of this material in the companion paper showed that this soft behavior and large work hardening rate was related to the inhomogeneous distribution of solute resulting from solidification, and related precipitate formation during the post-welding heat treatment. The stress–strain curve of the micro-sample in the fusion zone is actually close to the local stress–strain curve extracted by digital image correlation from the transverse tensile curve (see Figure 1), except that the failure strain is much lower in the micro-tensile sample, which can be explained by the change in sample geometry and constraint effect from the surrounding material in the weld.

B. *Implementation of the Local Elasto-plastic Constitutive Laws*

As suggested by the results obtained from the micro-tensile samples, from the hardness distribution and by the microstructure distribution shown in the companion paper,[50] it can be considered that the constitutive law for the totality of the HAZ until the edge of the FZ is similar to that of the base metal. It has been observed that during transverse testing, the HAZ remained elastic so that subtle differences in the strength of the different

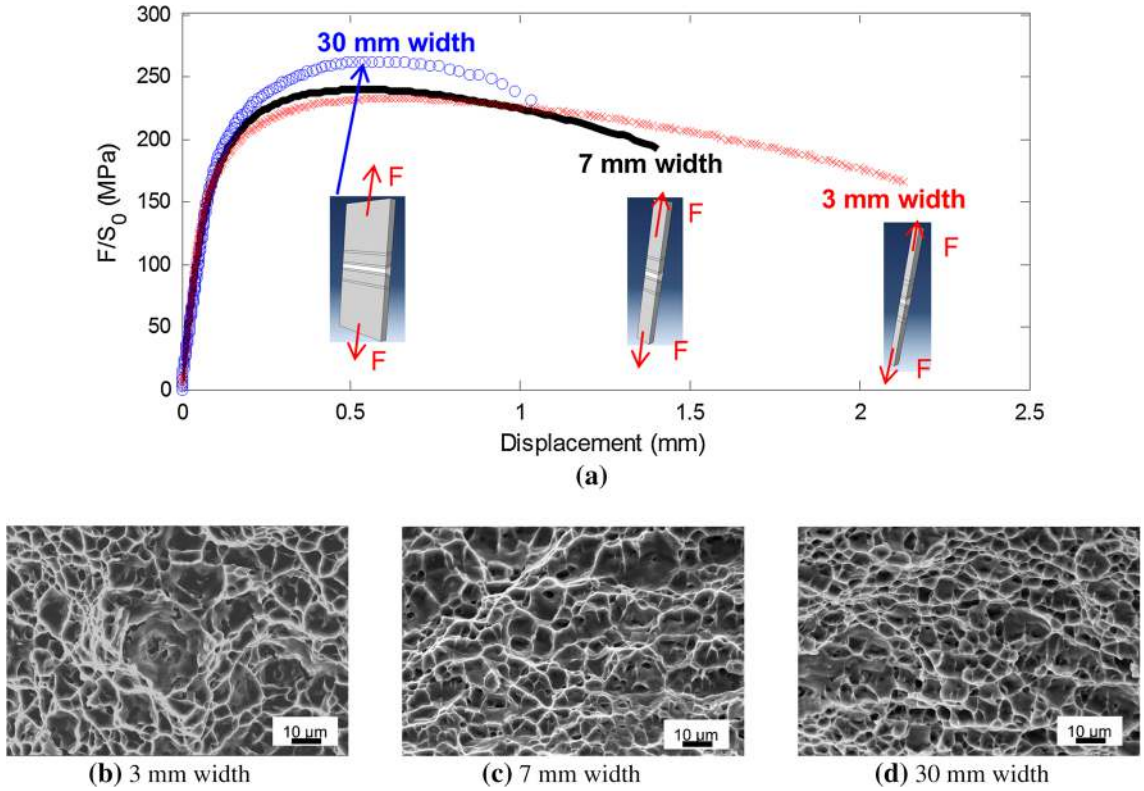

Fig. 4—(*a*) Nominal stress–displacement curves for the transverse tensile tests with three different sample width (3, 7 and 30 mm); (*b*) (*c*) and (*d*) SEM observations of the fracture surfaces for the same three samples showing a similar dimple distribution.

sub-regions of the HAZ (such as observed at 6 mm from the FZ) are not expected to influence the modeling results.

As a first trial, the weld assembly was therefore simply modeled by the superposition of two materials, one having the plastic behavior of the base metal, and the other of the fusion zone (Figure 7(a), subsequently called *without transition zone*). Concerning the base material, tensile tests were carried out in both directions of the plate (longitudinal and transverse), resulting in a relative difference smaller than 10 pct in the value of flow stress at any plastic strain. Therefore, the elasto-plastic constitutive law determined by the micro-tensile samples (longitudinal sample) was used for describing the transverse test. For the fusion zone, it is more difficult to make such a comparison, however the grain structure coming from solidification is isotropic so that applying the longitudinal constitutive law to the transverse modeling can also be considered to be a reasonable assumption. However, one difficulty for the fusion zone was that the deformation to fracture in the micro-tensile sample is of the order of 10 pct while the same zone deforms more than 30 pct when present in the weld assembly. The stress–strain curve needs therefore to be extrapolated to larger plastic strains. As compared to the base material, the fusion zone has a quite specific plastic behavior, with a very high initial strain hardening rate, related to its heterogeneous nature consisting of soft and hard zones. In order to describe properly the stress–strain curve to large strains, we used an isotropic Voce type hardening law; a description with two contributions that captured the specific stress–strain response better. The parameters (Q_1, b_1) and (Q_2, b_2) were identified from a least squares minimization procedure.

$$\sigma = \sigma_0 + Q_1\left(1 - \exp\left(-b_1\varepsilon_p\right)\right) + Q_2\left(1 - \exp\left(-b_2\varepsilon_p\right)\right) \quad [1]$$

with $\sigma_0 = 89.9$ MPa, $Q_1 = 115.1$ MPa, $b_1 = 24.3$, $Q_2 = 60$ MPa, $b_2 = 486.7$. The resulting stress–strain curve is shown in Figure 6 together with the experimental one.

Using the zone geometry defined in Figure 7(a) and the associated finite element mesh shown in Figure 7(c), the elasto-plastic behavior has been modeled. The dimension of the fusion zone was determined from optical microscopy measurements. The geometry of the tensile specimen was the same as that used for the experimental study, namely a thickness of 3 mm, a length of 60 mm, and a width varying between 3 and 30 mm.

The choice of the 3D modeling of the full specimen is guided by the asymmetry of the shape of the FZ in the thickness of the sample and by the fact that we aim to simulate the damage evolution in the sample. For the flat tensile samples, one end of the tensile sample is fully constrained whereas the displacement is imposed at the other end. The load is measured by summing the reaction force of all nodes on the end surface and the displacement is measured between two points that encompass the entire deformed region. The computation

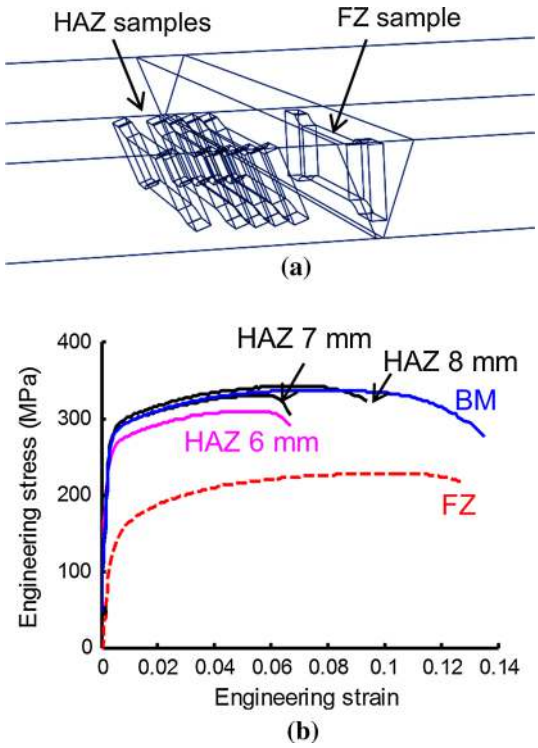

Fig. 5—(*a*) position of the micro-tensile samples with respect to the fusion zone; (*b*) nominal stress–strain curves for the micro-tensile samples in the different zones of the weld assembly.

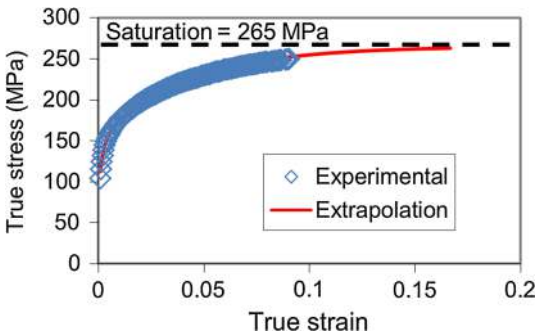

Fig. 6—True stress–strain curve of the micro-tensile sample in the fusion zone and extrapolation using the model described in the text.

is conducted using an explicit scheme. When the condition for failure is met locally, the corresponding element is removed (element deletion).

Figures 8(a) and (b) show the distribution of plastic strain across the weld at two different stages of the transverse tensile test (*curve without transition zone*). In both cases, although the average values of plastic strain within the weld nugget are correctly predicted, the detailed shape of the plastic strain distribution, showing some peaks distant from the center, is not in agreement with the DIC measurement. Moreover the macrosopic load–displacement curve is not well-described either.

In order to better describe the transition of mechanical properties between the base material and the weld nugget, we propose to introduce a transition zone of 1 mm with intermediate properties. This zone corresponds qualitatively to the observed fact (see companion paper[50]) that the precipitate distribution changes continuously with distance from the fusion zone. The mechanical behavior in this transition zone is taken similar to the one in the FZ, but shifted 30 MPa higher. With this adjustment, the new model geometry is shown in Figure 7(b), and the distribution in strain predicted by the model is compared to the experimental observation by digital image correlation in Figures 8(a) and (b). In this case the distribution of strain corresponds within experimental error to the observations. Figure 9 shows the comparison between the experimental and modeled load–displacement curves for the transverse test on the weld assembly. The predicted stress versus strain response is quite close to the experimental one until the maximum stress is reached. Then the load is slightly overestimated, and naturally no fracture point appears as no damage model is implemented yet. This discrepancy has to be fixed by the addition of the damage and fracture model, introduced in the following part.

C. *Micro-mechanically Based Damage Model: Gurson–Tvergaard–Needleman (GTN)*

The GTN[12] model is used to describe the material's poroplasticity, damage by void growth, and failure by void coalescence. When voids are initially present in the material, a continuum description of its poroplasticity is derived from the plastic potential Φ and related yield surface

$$\Phi = \frac{\sigma_{eq}^2}{\sigma_y^2} + 2q_1 f^* \cosh\left(\frac{3q_2}{2}\frac{\sigma_m}{\sigma_y}\right) - \left(1 + q_1^2 f^{*2}\right) = 0, \quad [2]$$

where σ_{eq} is the equivalent von Mises stress, σ_y the current yield stress, σ_m the mean stress, the material being elastic–plastic with an isotropic hardening given by [1]. The term f^* represents the effective void volume fraction as defined below. The parameters q_1 and q_2 control the profile of the yield surface in the $\sigma_{eq} - \sigma_m$ diagram. When q_1 equals zero, Φ reduces to the classical rate independent J_2-flow theory; the case $q_1 = q_2 = 1$ corresponds to the initial Gurson model.[11] Detailed periodic unit cell calculations by Tvergaard[13,51,52] have shown that the values $q_1 = 1.5$ and $q_2 = 1$ better capture the yield surface [2], at least for a material with a hardening exponent equal to 0.1, which is approximately found from [1]. Detailed calibrations of the q_i are reported by Koplik and Needleman[53] and Faleskog et al.[54] These result in the ranges $1.2 \le q_1 \le 2$ and $q_2 \simeq 1$. Considering this, we used in our model $q_1 = 1.5$ and $q_2 = 1$. These values correspond to classical values for a ductile metal and are not specific to the material studied here.

The initial Gurson model assumes the growth of spherical voids by plastic deformation of the matrix up to the critical porosity $f_u = 1/q_1 = 1$. This is unrealistically large in most metals, in particular because void coalescence that follows the first stages of the increase in porosity involves non-spherical void growth and localization of plastic deformation. To account for this effect, Needleman and Tvergaard[12] proposed to use a function $f^*(f)$ to describe void growth and coalescence as

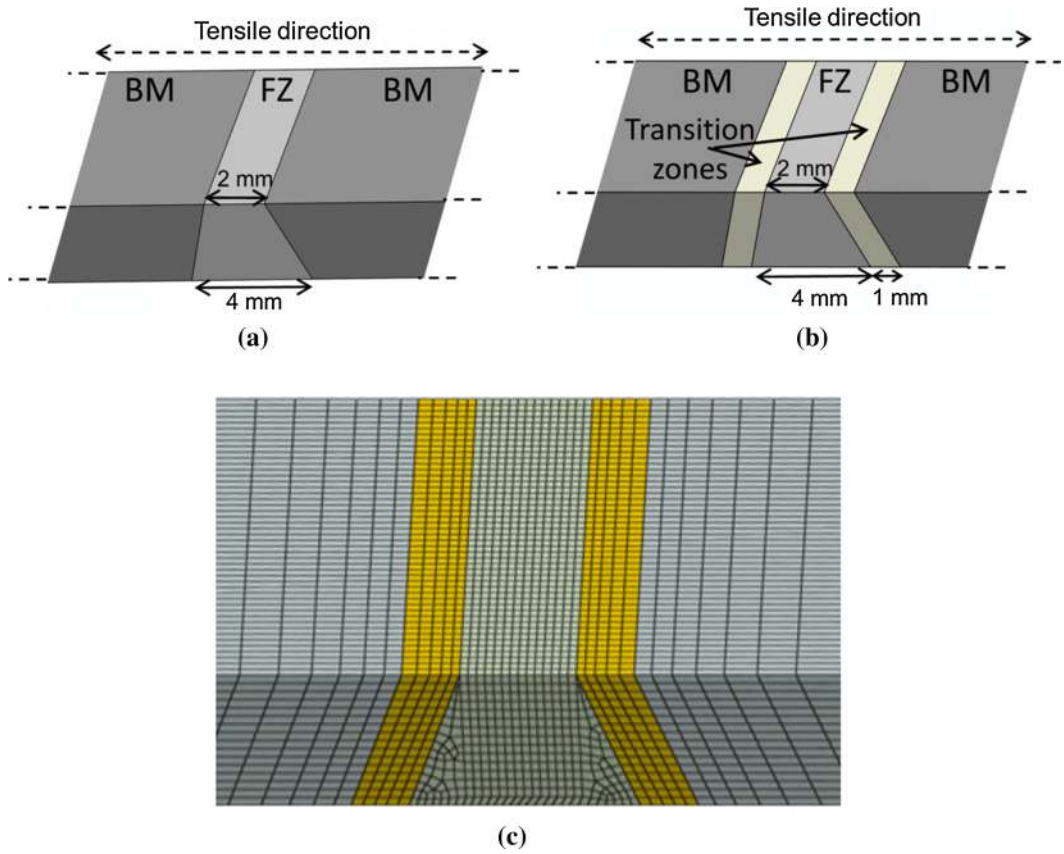

Fig. 7—(*a*) Model geometry for the transverse tensile sample defined with two materials (fusion zone and base metal); (*b*) Model geometry for the transverse tensile sample defined with three materials (fusion zone, transition zone and base metal); (*c*) Geometry of the finite element mesh used for the transverse tensile test.

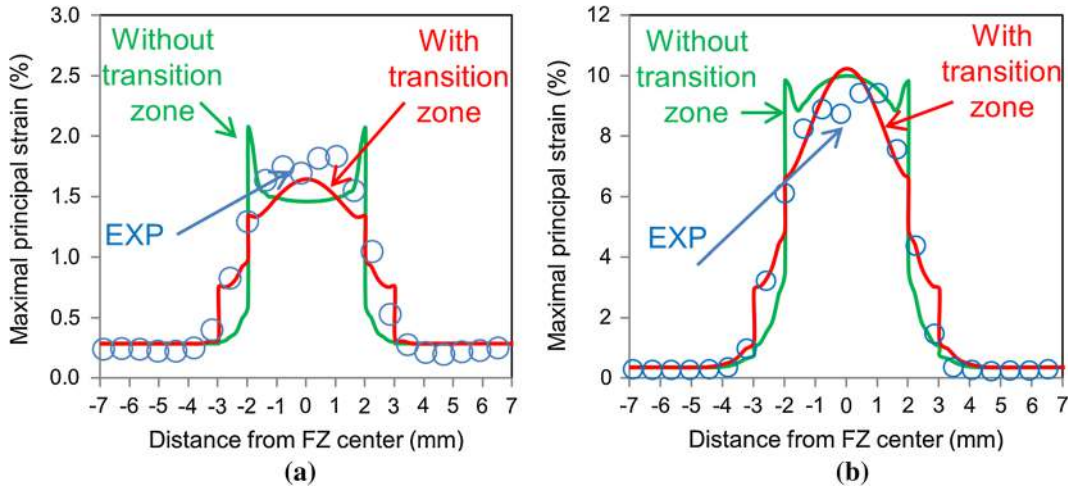

Fig. 8—(*a*) and (*b*) Comparison between the experimental distributions of strain as measured by digital image correlation and as predicted by the model for two different stages of the tensile tests. The result of the model is presented both for the model using two material properties (without transition zone) and the one using three material properties (with transition zone).

$$\begin{cases} f^* = f & \text{for} \quad f < f_c \\ f^* = \delta(f - f_c) + f_c & \text{for} \quad f \geq f_c \end{cases}, \qquad [3]$$

up to the ultimate porosity $f_u^* = 1/q_1$. In [3], the porosity growth rate is increased by a factor of $\frac{f_u - f_c}{f_F - f_c}$ once void volume fraction reaches f_c. The value of f_c is observed to depend mainly on the initial porosity[53] and little on the mean stress and in general $f_c < 0.15$.[12] Thus, the void growth and coalescence model [3] is fully determined by the values of f_c and f_u. In the region where damage takes place, the mesh size is fixed with brick elements of

0.15 mm long edges. The size is kept the same for all tests reported. Damage calculations involve softening, that results in mesh-size dependence of the predictions. A non-local approach could be employed to overcome this. We preferred a more practical approach that consists in using the same mesh for all calculations. The parameters identified in the following are thus related to the discretization adopted but still capture the underlying physics.

In the damage simulation, we consider that there is no nucleation step for voids, but that voids already exist in the unstrained material. This choice is supported by the observation made about the structure of the damage nucleation sites. These sites are constituted by the Fe-rich intermetallic particles, according to our former hypothesis. As mentioned in the companion paper,[50] these particles are in fact constituted of incoherent aggregates of nano-crystals, which under positive hydrostatic pressure should not oppose any resistance to void growth. In addition, the fact that the dimple size does not appear to depend on hydrostatic pressure (see Figure 4) is consistent with the hypothesis of pre-existing damage.

In summary, only three parameters need to be determined in the model of damage evolution, namely: the initial void volume fraction $f_{0,}$ the critical void volume fraction at coalescence $f_{c,}$ and the void volume fraction at fracture f_F.

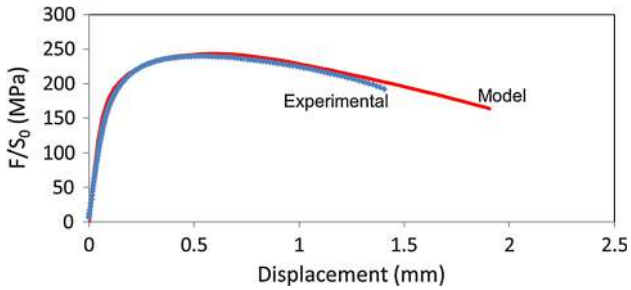

Fig. 9—Comparison between the experimental and modeled nominal stress-displacement curve for the 7 mm wide transverse tensile test. The model at this stage only includes the elasto-plasticity without damage.

D. *Parameter Evaluation*

The Fe-rich intermetallic particles are considered as an initial porosity. To estimate the volume fraction occupied by these particles, we applied a thresholding method to ten SEM images, obtained in the same conditions. To avoid subjectivity in the choice of the threshold, an automatic method based on entropy maximization was chosen (from the ImageJ image analysis software). With this method, a value of 0.7 pct of surface fraction was found. It is assumed that the volume fraction is equivalent to the surface fraction.

The coalescence parameters were then adjusted through a parametric study of their influence on the 7-mm-width flat sample. According to the literature,[12,13] the calibration of the void growth model [3] accounts for the limits for f_c in the range 1 to 15 pct and f_u in the range 15 to 25 pct. On Figure 10(a) it is shown that in the range of the assumed values, the fracture point occurs relatively close to the experimental one, and that for f_c = 5 pct, this point is very well reproduced. On the other hand, with the chosen value of f_c (5 pct), the model shown is mostly insensitive to the value of the parameter f_F (Figure 10(b)), which we adjusted at 20 pct.

E. *Results for Different Sample Geometry*

The set of parameters that has been adjusted to the above-mentioned sample geometry is used to model the other flat-tensile samples, with the different widths. The results are presented in Figure 11(a) (lines) and compared to the experimental curves (markers). The model follows the experimental trends with good accuracy: the apparent yield stress increases with the width, whereas the strain to fracture decreases. Some remaining discrepancies are observed such as a slightly underestimated strain to fracture for the 30-mm-width sample, and an overestimated load drop after necking for the 3-mm-width sample.

The different responses obtained when the width is varied are most probably due to a change in the stress state generated in the FZ during the loading, a side effect of the plastic localization in this zone. This variation of

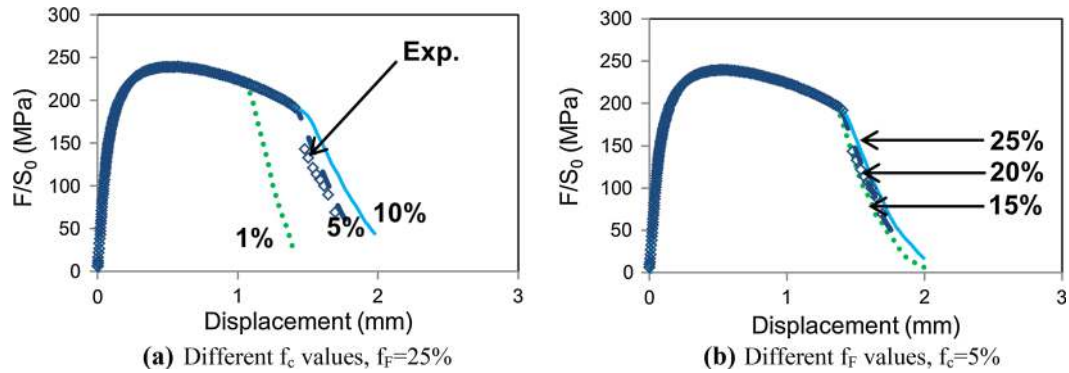

Fig. 10—Comparison between the experimental and modeled nominal stress-displacement curve for the 7 mm wide transverse tensile test using the model with damage evolution for different values of the model parameters. (*a*) Varying fraction of coalescence initiation for a fracture fraction of 25 pct; (*b*) varying fracture fraction for a coalescence initiation fraction of 5 pct.

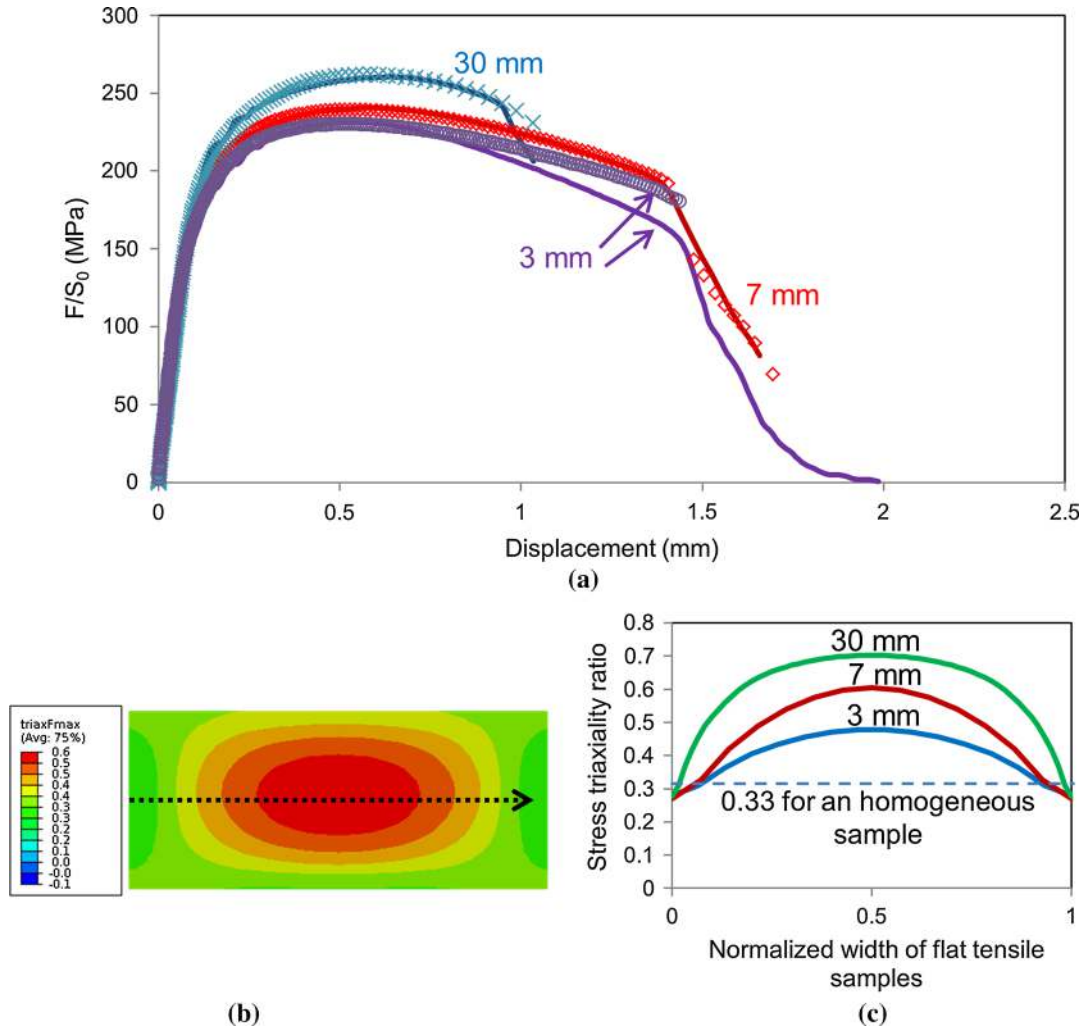

Fig. 11—(*a*) Comparison between the experimental and modeled nominal stress-displacement curves for the different sample widths; (*b*) distribution of stress triaxiality ratio in the middle cross-section of the 7 mm wide transverse tensile test; (*c*) distribution of stress triaxiality ratio along the sample width (normalized to 1) at maximum load for the three samples of width 3, 7 and 30 mm.

the stress state is characterized by the stress triaxiality ratio (STR), which is the ratio of the mean stress σ_m to the equivalent von Mises stress: $\eta = \frac{\sigma_m}{\sigma_{eq}}$. Figure 11(b) presents the map of the STR in the middle section of the 7-mm-wide sample at maximum load. This map shows that the maximum STR is located close to the center of the sample (note that the slight asymmetry of the distribution of STR is due to the asymmetry of the nugget geometry). The profiles of STR at middle thickness, calculated at maximum load for each flat-tensile sample are plotted in Figure 11(c) as a function of the normalized position along the sample width. As a reference, the STR existing in a homogeneously deforming tensile sample before is represented. As expected the plastic localization exerts a constraint on the fusion zone that results in an increasing STR as a function of sample width, up to 0.7 for the 30-mm-wide sample.

An even higher degree of plastic constraint can be reached in a notched sample such as that used for the Kahn tear tests. Therefore, in order to evaluate the robustness of the model toward higher degrees of plastic constraint, a Kahn tear test was both experimentally carried out, with the notch positioned in the middle of the weld nugget, and modeled using the same parameters as that of the tensile samples. Figures 12(a) and (b) show respectively the geometry of the Kahn tear sample and the mesh that was used for modeling it. Figure 12(c) shows the experimental load–displacement curve of the Kahn tear test and the prediction of the model. The agreement between the two is particularly accurate. Figure 12(d) shows the distribution of strain predicted by the model at maximum load. Similar to the transverse tensile test, the plastic strain is fully localized in the weld nugget and the base metal remains elastic. Figure 12(e) shows the distribution of stress triaxiality calculated along the sample section before fracture propagation occurs. Values above 1 are reached in this sample geometry.

A side result of the Kahn tear test is the calculation of the unit initiation energy (UIE) and the unit propagation energy (UPE),[55] which are representative of the toughness of the assembly. The UIE is the energy dissipated during the Kahn Tear Test before maximum load and the UPE, the dissipated energy after maximum

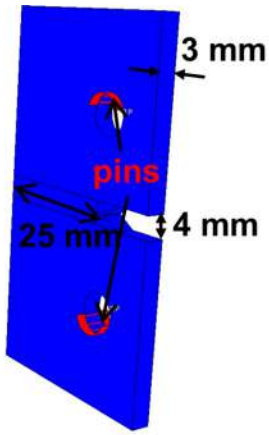
3 mm
pins
25 mm
4 mm

(a)

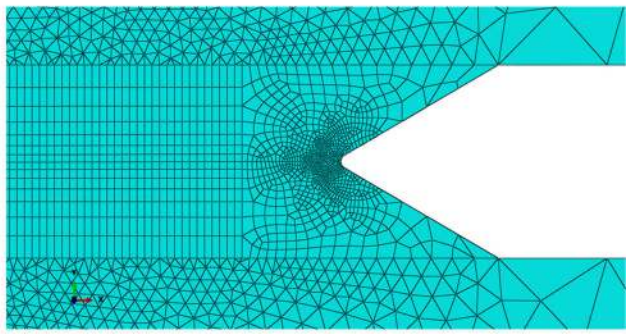

(b)

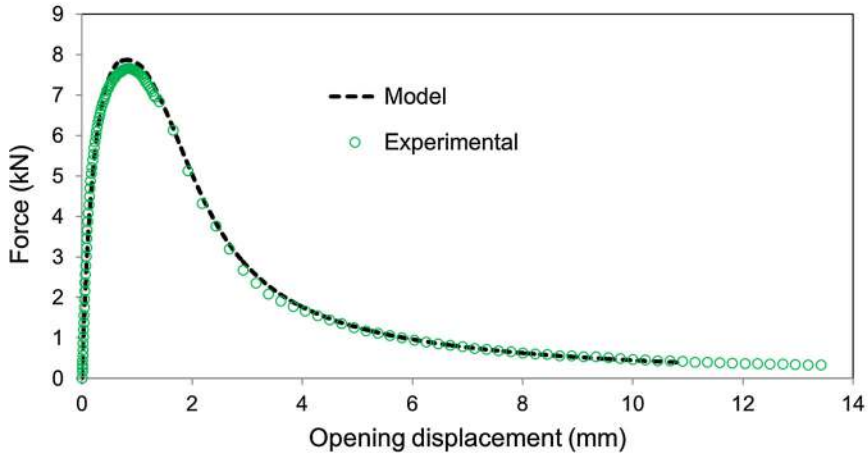
Force (kN)
Opening displacement (mm)
Model
Experimental
0
1
2
3
4
5
6
7
8
9
0
2
4
6
8
10
12
14

(c)

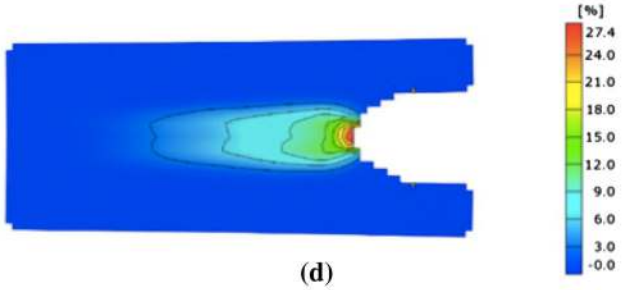
[%]
27.4
24.0
21.0
18.0
15.0
12.0
9.0
6.0
3.0
-0.0

(d)

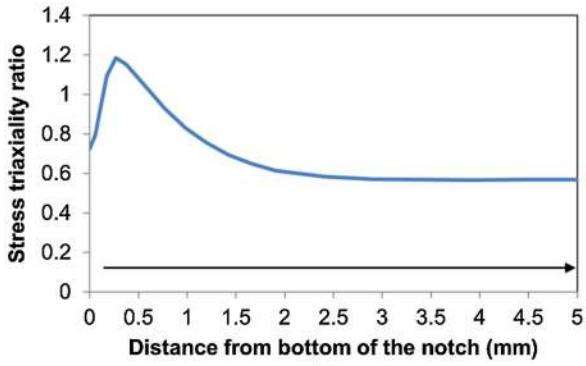
Stress triaxiality ratio
Distance from bottom of the notch (mm)
0
0.2
0.4
0.6
0.8
1
1.2
1.4
0
0.5
1
1.5
2
2.5
3
3.5
4
4.5
5

(e)

◀Fig. 12—(*a*) geometry of the Kahn tear test sample; (*b*) Mesh geometry in the notch region; (*c*) Comparison between the experimental and modeled load–displacement curves; (*d*) strain distribution close to the notch predicted by the model at maximum load; (*e*) Distribution of stress triaxiality ratio from the edge of the notch before the propagation of fracture.

load. For the welded material, the UIE is of the order of 60 kJ m^{-2} and the UPE is of the order of 290 kJ m^{-2}. As a comparison, the values for the base metal are respectively (UIE = 95, UPE = 390, same units) for longitudinal testing (crack propagating in the transverse direction) and (UIE = 55, UPE = 140, same units) for transversal testing (crack propagating in the longitudinal direction). These results suggest that the fusion zone, embedded in the base metal, exhibits a comparable toughness as compared to the base metal, meaning that the fine grain structure and high ductility of the fusion zone ensures a large plastic dissipation ability.

V. DISCUSSION

In the companion paper, a detailed analysis of the microstructure of the EN-AW 7020 electron beam weld was carried out. It was shown that the spatial distribution of microstructure showed several degrees of complexity.

First, as with any welding technique, the material possesses a heat-affected zone after the welding operation, as evidenced by the microstructure in the naturally aged condition. Namely, the hardening precipitates initially present were all dissolved in a wide region outside the weld nugget, and some coarsening was observed in the transition region between the undissolved and dissolved precipitates. However, the assembly was subsequently heat treated to a T6 condition, which resulted in an almost homogeneous distribution of mechanical properties throughout the HAZ until the unaffected base material. This homogeneity of microstructure can be related to the relatively low solute content of the alloy, which is consequently relatively quench-insensitive, and can recover a full strength after heat treatment. In the present paper, it has been observed that the heat-affected zone remained elastic until fracture of the weld nugget. Therefore, the details of microstructure distribution in the HAZ do not appear to play a role in the mechanical behavior of the assembly, and for our purpose the material outside the fusion zone could be considered to show a uniform behavior.

Secondly, the microstructure within the weld nugget was shown to be relatively complex, resulting from the nugget solidification and subsequent T6 heat treatment. At the cores of the solidification cells (or dendrites), the solute content was observed to be sufficiently large so that a uniform distribution of precipitates could be formed after the heat treatment. In the inter-dendritic regions, however, the solute content is very low, and the material is completely free of precipitates after heat treatment, resulting in a very heterogeneous microstructure and related hardness distribution at the micrometer scale. Finally, in the regions that solidify last, clusters of loosely packed Fe-containing nanocrystals were observed. These clusters, which are located at the core of the hardest regions of the weld nugget, provide natural sites for ductile damage initiation.

The heterogeneous nature of the microstructure, at the micron scale, of the weld nugget results in a high strain hardening rate due to an extended elastic–plastic transition, as can be observed in the micro-tensile stress–strain curve in Figure 5. This feature can be straightforwardly taken into account by adjusting the strain-hardening curve parameters in the model. However, it could also be expected to influence the local stress state in the hard and soft zones of the microstructure, especially in the vicinity of the damage initiation sites. Similarly, the effect of the soft Precipitate-Free Zones around the grain boundaries in precipitation hardening alloys on damage initiation has been evidenced in the literature.[56] However, we have shown in the present work that a simple model, taking only into account the macroscopic stress state imposed by the harder parent material on the softer weld nugget, was sufficient to describe the evolution of damage and resulting ductility in a wide range of stress conditions, where the stress triaxiality ratio was varied from 0.45 (3 mm sample) to more than 1 (Kahn tear test), the latter values being particularly relevant to describe the ductile fracture of the weld assembly under conditions of crack propagation involving generalized plasticity of the weld zone.

It may be interesting to note that the strongest discrepancy between the experimental results and the model was observed for the sample where the macroscopic triaxiality ratio was the lowest (3 mm sample). Although it is not straightforward to understand why in this case the model would underestimate the stress evolution (and thus overestimate the damage accumulation), it may be a sign that when the macroscopic triaxiality is low, the effect of a microscopic distribution of triaxiality should be considered. In order to quantify the effect of the spatial distribution of strength on the evolution of damage, unit cell calculations could be performed, where the morphology and properties of the hard and soft zones could be varied independently.

VI. CONCLUSIONS

In this paper we presented a systematic study of the mechanical behavior of an electron beam welded 7020 Aluminum alloy in the heat-treated condition, where the sample geometry has been varied so that a wide range of stress states was tested, resulting in a range of stress triaxiality ratio from 0.45 to 1.3. The combination of the experimental study and the finite element simulation including a model for ductile damage evolution leads to the following conclusions:

1. In the heat-treated temper, the complexity of the weld microstructure evidenced in the companion paper can be simplified to the combination of a uniform parent material, which remains elastic during the loading of the assembly, and of the weld nug-

get, which is much softer but shows a high strain-hardening rate due to its heterogeneous distribution of precipitates and the microscopic scale. Adding a small transition zone between these two materials proved to be necessary to describe properly the strain distribution.

2. Damage pre-existed in the weld nugget in the form of loosely packed clusters of Fe-containing nano-particles. These particles were the basis for the growth and coarsening of voids leading to ductile fracture.
3. A finite element model based on the individual stress–strain curves of the constitutive materials of the assembly and including a void evolution model was successful at describing the evolution of damage in a wide range of stress states, without the need for a damage nucleation model, and despite the fact that the complexity of the spatial distribution of strength was not accounted for.
4. Changing the sample cross-section, namely the sample width at constant thickness, has proven an efficient way of imposing a varying amount of constraint on the soft weld zone, and therefore helping to assess the robustness of the model developed.

REFERENCES

1. G. Mathers: *The Welding of Aluminium and Its Alloys*, Woodhead Publishing, Cambridge, UK, 2002.
2. T. Ma and G. den Ouden: *Mater. Sci. Eng. A*, 1999, vol. A266, pp. 198–204.
3. G. Cam and M. Kocak: *J. Mater. Sci.*, 2007, vol. 42, pp. 7154–61.
4. G.D.J. Ram, T.K. Mitra, V. Shankar, and S. Sundaresan: *J. Mater. Process. Technol.*, 2003, vol. 142, pp. 174–81.
5. W.D. Lockwood, B. Tomaz, and A.P. Reynolds: *Mater. Sci. Eng. A*, 2002, vol. 323, pp. 348–53.
6. W.D. Lockwood and A.P. Reynolds: *Mater. Sci. Eng. A*, 2003, vol. 339, pp. 35–42.
7. C. Genevois, A. Deschamps, and P. Vacher: *Mater. Sci. Eng. A*, 2006, vol. A415, pp. 162–70.
8. T. Wang, O.S. Hopperstad, P.K. Larsen, and O.-G. Lademo: *Comput. Struct.*, 2006, vol. 84, pp. 2016–32.
9. A.A. Zadpoor, J. Sinke, and R. Benedictus: *Metall. Mater. Trans. A*, 2010, vol. 41A, pp. 3365–78.
10. D. Rao, K. Huber, J. Heerens, J.F. dos Santos, and N. Huber: *Mater. Sci. Eng. A*, 2013, vol. 565, pp. 44–50.
11. A.L. Gurson: *J. Eng. Mater. Technol.*, 1977, vol. 99, pp. 2–15.
12. A. Needleman and V. Tvergaard: *J. Mech. Phys. Solids*, 1984, vol. 32, pp. 461–90.
13. V. Tvergaard: *Adv. Appl. Mech.*, 1990, vol. 27, pp. 83–151.
14. M. Gologanu, J.B. Leblond, G. Perrin, and J. Devaux: *Continuum Micromechanics*, Springer Verlag, Berlin, 1995, pp. 61–106.
15. T. Pardoen and J.W. Hutchinson: *J. Mech. Phys. Solids*, 2000, vol. 48, pp. 2467–512.
16. T. Pardoen and J.W. Hutchinson: *Acta Mater.*, 2003, vol. 51, pp. 133–48.
17. A.A. Benzerga, J. Besson, and A. Pineau: *Acta Mater.*, 2004, vol. 52, pp. 4639–50.
18. M. Hval, C. Thaulow, J.H. Lange, S.H. Hoydal, and Z.L. Zhang: *Weld. J.*, 1998, vol. 77, pp. 208S–17S.
19. P. Negre, D. Steglich, and W. Brocks: *Eng. Fract. Mech.*, 2004, vol. 71, pp. 2365–83.
20. C. Gallais, A. Simar, D. Fabregue, A. Denquin, G. Lapasset, B. de Meester, Y. Brechet, and T. Pardoen: *Metall. Mater. Trans. A*, 2007, vol. 38A, pp. 964–81.
21. A. Nonn, W. Dahl, and W. Bleck: *Eng. Fract. Mech.*, 2008, vol. 75, pp. 3251–63.
22. D. Lassance, D. Fabrègue, F. Delannay, and T. Pardoen: *Prog. Mater Sci.*, 2007, vol. 52, pp. 62–129.
23. T. Pardoen, F. Scheyvaerts, A. Simar, C. Tekoglu, and P.R. Onck: *C. R. Phys.*, 2010, vol. 11, pp. 326–45.
24. K.L. Nielsen, T. Pardoen, V. Tvergaard, B. de Meester, and A. Simar: *Int. J. Solids Struct.*, 2010, vol. 47, pp. 2359–70.
25. R. Chhibber, P. Biswas, N. Arora, S.R. Gupta, and B.K. Dutta: *Int. J. Fract.*, 2011, vol. 167, pp. 71–82.
26. A. Simar, K.L. Nielsen, B. de Meester, V. Tvergaard, and T. Pardoen: *Eng. Fract. Mech.*, 2010, vol. 77, pp. 2491–2503.
27. A. Simar, Y. Brechet, B. de Meester, A. Denquin, C. Gallais, and T. Pardoen: *Prog. Mater Sci.*, 2012, vol. 57, pp. 95–183.
28. S. Tosto, F. Nenci, and J. Hu: *Mater. Sci. Technol.*, 1996, vol. 12, pp. 323–28.
29. E. Ciompi and A. Lanciotti: *Eng. Fract. Mech.*, 1999, vol. 62, pp. 463–76.
30. Y. Sakamoto, M. Terabayashi, N. Kazita, S. Sanuki, T. Mae, H. Notoya, and K. Arai: *J. Jpn. Inst. Met.*, 1999, vol. 63, pp. 924–30.
31. Y. Sakamoto, C. Shibuta, S. Sanuki, T. Mae, H. Notoya, and K. Arai: *Mater. Trans. JIM*, 1999, vol. 40, pp. 556–63.
32. S.C. Chen and J.C. Huang: *Mater. Sci. Technol.*, 1999, vol. 15, pp. 965–78.
33. S.C. Chen and J.C. Huang: *Mater. Trans. JIM*, 1999, vol. 40, pp. 1069–78.
34. C.H. Lee, S.W. Kim, and E.P. Yoon: *Sci. Technol. Weld. Join.*, 2000, vol. 5, pp. 277–83.
35. G. Cam, V. Ventzke, J.F. Dos Santos, M. Kocak, G. Jennequin, P. Gonthier-Maurin, M. Penasa, C. Rivela, and D. Boisselier: *Prakt. Metallogr.*, 2000, vol. 37, pp. 59–89.
36. S.R.K. Rao, G.M. Reddy, K.S. Rao, M. Kamaraj, and K.P. Rao: *Mater. Charact.*, 2005, vol. 55, pp. 345–54.
37. B.S. Nair, G. Phanikumar, K. Prasad Rao, and P.P. Sinha: *Sci. Technol. Weld. Join.*, 2007, vol. 12, pp. 579–85.
38. S. Malarvizhi, K. Raghukandan, and N. Viswanathan: *Int. J. Adv. Manuf. Technol.*, 2008, vol. 37, pp. 294–301.
39. A. Deschamps, S. Ringeval, G. Texier, and L. Delfaut-Durut: *Mater. Sci. Eng. A*, 2009, vol. 517, pp. 361–68.
40. P. Wanjara and M. Brochu: *Vacuum*, 2010, vol. 85, pp. 268–82.
41. B.S. Nair, S. Rakesh, G. Phanikumar, K. Prasad Rao, and P.P. Sinha: *Mater. Des.*, 2010, vol. 31, pp. 4943–50.
42. D. Maisonnette, M. Suery, D. Nelias, P. Chaudet, and T. Epicier: *Mater. Sci. Eng. A*, 2011, vol. 528, pp. 2718–24.
43. M. Pakdil, G. Cam, M. Kocak, and S. Erim: *Mater. Sci. Eng. A*, 2011, vol. 528, pp. 7350–56.
44. S. Malarvizhi and V. Balasubramanian: *J. Mater. Eng. Perform.*, 2011, vol. 20, pp. 359–67.
45. S. Malarvizhi and V. Balasubramanian: *Weld. World*, 2012, vol. 56, pp. 105–19.
46. V.R. Skal's'kyi and I.M. Lyasota: *Mater. Sci.*, 2010, vol. 46, pp. 115–23.
47. V.R. Skal's'kyi, D.V. Rudavs'skyi, and I.M. Lyasota: *Mater. Sci.*, 2012, vol. 48, pp. 355–63.
48. S. Kim, Y. Jeong, J. Park, and Y. Lee: *J. Mech. Sci. Technol.*, 2013, vol. 27, pp. 2935–40.
49. A.D. Zervaki, V. Stergiou, and S.G. Lambrakos: *J. Mater. Eng. Perform.*, 2013, vol. 22, pp. 3175–81.
50. Q. Puydt, S. Flouriot, S. Ringeval, F. De Geuser, G. Parry, and A. Deschamps: *Metall. Mater. Trans. A*, 2014, DOI: 10.1007/s11661-014-2566-9.
51. V. Tvergaard: *Int. J. Fract.*, 1981, vol. 17, pp. 389–407.
52. V. Tvergaard: *J. Mech. Phys. Solids*, 1982, vol. 30, pp. 265–86.
53. J. Koplik and A. Needleman: *Int. J. Solids Struct.*, 1988, vol. 24, pp. 835–53.
54. J. Faleskog, X.S. Gao, and C.F. Shih: *Int. J. Fract.*, 1998, vol. 89, pp. 355–73.
55. D. Dumont, A. Deschamps, and Y. Brechet: *Mater. Sci. Eng. A*, 2003, vol. 356, pp. 326–36.
56. T. Pardoen, D. Dumont, A. Deschamps, and Y. Brechet: *J. Mech. Phys. Solids*, 2003, vol. 51, pp. 637–65.